Method for traveling-wave deceleration of buffer-gas beams of CH

M. I. Fabrikant,[1] Tian Li,[2,*] N. J. Fitch,[1] N. Farrow,[1] Jonathan D. Weinstein,[2] and H. J. Lewandowski[1]
[1]*JILA and Department of Physics, University of Colorado, Boulder, Colorado 80309-0440, USA*
[2]*Department of Physics, University of Nevada, Reno, Nevada 89557, USA*
(Received 2 December 2013; revised manuscript received 9 June 2014; published 17 September 2014)

Cryogenic buffer-gas beams are a promising method for producing bright sources of cold molecular radicals for cold-collision and chemical-reaction experiments. In order to use these beams in studies of reactions with controlled collision energies or in trapping experiments, one needs a method of controlling the forward velocity of the beam. A Stark decelerator can be an effective tool for controlling the mean speed of molecules produced by supersonic jets, but efficient deceleration of buffer-gas beams presents new challenges due to longer pulse lengths. Traveling-wave decelerators are uniquely suited to meet these challenges because of their ability to confine molecules in three dimensions during deceleration and their versatility afforded by the analog control of the electrodes. We have created ground-state CH($X\,^2\Pi$) radicals in a cryogenic buffer-gas cell with the potential to produce a cold molecular beam of 10^{11} molecules/pulse. We present a general protocol for Stark deceleration of beams with a large position and velocity spread for use with a traveling-wave decelerator. Our method involves confining molecules transversely with a hexapole for an optimized distance before deceleration. This rotates the phase-space distribution of the molecular packet so that the packet is matched to the time-varying phase-space acceptance of the decelerator. We demonstrate with simulations and an analytic one-dimensional model that this method can decelerate a significant fraction of the molecules in successive wells of a traveling-wave decelerator to produce energy-tuned beams for cold and controlled-molecule experiments.

DOI: 10.1103/PhysRevA.90.033418 PACS number(s): 37.10.Mn, 34.50.Lf

I. INTRODUCTION

Cryogenic buffer-gas methods have the potential to create bright beams of a large range of cold molecule species that have not yet been studied in depth because of the challenge of creating supersonic jets of these molecules [1,2]. There are several applications of intense molecular beams, from experiments attempting to measure the electron's electric dipole moment [3,4] and variation of fundamental constants [5] to experiments exploring cold reactions relevant to interstellar cloud chemistry [6]. In most of these experiments, removing the mean forward velocity is critical to taking full advantage of the molecular source. Over the last 10 years, many methods for molecular deceleration have been developed, with Stark deceleration being the most widely used technique [7]. However, no one has yet used a Stark decelerator to decelerate these intense buffer-gas beams. Thus far, experimental approaches for decelerating such beams have been limited to direct laser slowing [8] and combining magnetic potentials with optical pumping [9].

To demonstrate the advantages of a combined system of a buffer-gas beam with a Stark decelerator, we chose CH (methylidyne), the simplest organic molecule. As a radical, CH is difficult to create in the laboratory but plays an important role in interstellar medium chemistry and combustion chemistry. CH participates in archetypical reactions such as hydrogen exchange with deuterium [10],

$$\mathrm{CH}(X\,^2\Pi) + \mathrm{D_2} \rightarrow \mathrm{CD}(X\,^2\Pi) + \mathrm{HD}, \tag{1}$$

the formation of more complex hydrocarbons [11],

$$\mathrm{CH} + \mathrm{H_2} \rightarrow \mathrm{CH_3} + h\nu, \tag{2}$$

and simple combustion reactions [12],

$$\begin{aligned} \mathrm{CH}(X\,^2\Pi) + \mathrm{C_2H_2} &\rightarrow \mathrm{C_3H_2} + \mathrm{H}, \\ \mathrm{CH}(X\,^2\Pi) + \mathrm{C_2H_2} &\rightarrow \mathrm{C_3H} + \mathrm{H_2}. \end{aligned} \tag{3}$$

In the cold, dilute, interstellar medium, the most important reactions can be expected to be two-body barrierless reactions [13]. In order to study such reactions, the ability to prepare the reactants with extremely well known interaction energies is crucial. CH reactions have been studied in crossed-beam experiments [14] and at temperatures as low as 23 K [15], but collision experiments in which the CH beam is both internally cold and traveling at a low velocity remain unexplored. We propose that progress toward such experiments can be made by combining a molecular beam of CH with a Stark decelerator, which will allow us to create a cold, bright, controlled-velocity source of CH. In addition, molecules in a decelerated CH beam could potentially be combined and trapped with magnetic or electric fields. This would enable the study of collisions down to energies in the 10–100 mK regime with essentially only one quantum state populated [16].

This paper describes experimental work investigating the production of CH in a cryogenic buffer-gas cell and detailed calculations of the coupling of a cryogenic beam of CH to a traveling-wave Stark decelerator.

II. CRYOGENIC PRODUCTION OF CH

We produce methylidyne (CH) by laser ablation of a solid target and cool it with a cryogenic helium buffer gas. The experimental apparatus and techniques are as described in Ref. [17]. The cryogenic cell in which the experiment takes

*Present address: Joint Quantum Institute, National Institute of Standards and Technology and the University of Maryland, College Park, MD 20742, USA.

place is modified from that reference to have an internal volume of roughly $10 \times 10 \times 2.5$ cm.

We chose iodoform (CHI_3) as the solid precursor in the hopes that the weak C-I bond would favor the formation of CH in ablation, inspired by prior work producing CH from photolysis of gas-phase bromoform [18]. We obtained iodoform in powder form; to form suitable targets for ablation, we dissolved iodoform powder (99% purity) in acetone and let the acetone evaporate to leave a solid on a metal substrate. However, the targets that produced the observed signal turned a blackish color after evaporation (changed from the original yellowish powder color), suggesting that the chemical composition of the ablation target is no longer pure iodoform.

We detect the cold methylidyne molecules by laser absorption spectroscopy. Typical probe beam powers are on the order of a few microwatts, with a probe beam diameter of a few millimeters. We observe CH molecules in the $X\,^2\Pi(v'' = 0, N'' = 1, J'' = 1/2)$ rovibrational ground state on the $B\,^2\Sigma^- \leftarrow X\,^2\Pi$ Q- and P-branch transitions at 389 nm [19]. The spectra are shown in Fig. 1. We note that we are unable to resolve the ground-state hyperfine structure and that parity-selection rules prevent measurement of the λ doubling in the ground state [20].

The two peaks observed on the Q-branch transition are due to the spin-rotation splitting of the $J' = 1/2$ and $J' = 3/2$ states of the $B\,^2\Sigma(N' = 1)$ excited state. The P-branch transition to the $B\,^2\Sigma(N' = 0, J' = 1/2)$ state shows only a single absorption peak.

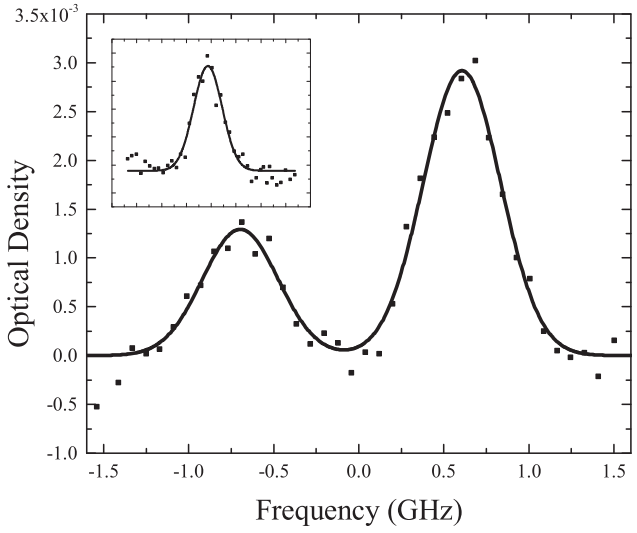

FIG. 1. Spectra of $X\,^2\Pi(v'' = 0, N'' = 1, J'' = 1/2)$ cryogenic CH molecules. The main figure shows the Q-branch transitions; the frequency offset is 25 723.4 cm^{-1}. The inset shows the P-branch transition plotted on the same scale; its frequency offset is 25 698.2 cm^{-1}. The spectra were obtained from 1 to 2 ms after the ablation pulse. The experimental measurements are shown as points, and the fit to a Gaussian (two Gaussians in the case of the Q-branch transition) is shown as a solid line. The data were taken at a cell temperature of 5 K, ablation energy of 0.1 J, and helium buffer gas density of 1×10^{16} cm^{-3}.

The relative heights of the three peaks are consistent with calculated absorption coefficients [21].

From these spectra, we calculate that we produce 2×10^{11} CH molecules in each of the λ-doublet states of $X\,^2\Pi(v'' = 0, N'' = 1, J'' = 1/2)$ [21].

Similar numbers are observed for helium buffer-gas densities from 4×10^{15} to 1×10^{17} cm^{-3}. We note that high-flux cryogenic buffer-gas beam sources typically employ buffer-gas densities from 10^{15} to 10^{16} cm^{-3} [22].

The measured temperature for the data shown in Fig. 1 is 17 ± 2 K, which is significantly higher than the 5 K cell wall temperature measured prior to ablation. This can be attributed to the large ablation power and short observation time after the laser pulse [23]. Lower ablation powers of 0.05 J showed temperatures of 13 ± 1 K. We ultimately intend to use a neon buffer gas in our source because neon is significantly easier to cryogenically pump, which will give us a lower pressure in the deceleration chamber and a longer running time before we have to regenerate the cryogenic sorb. While the increase in temperature might be quite deleterious for a helium-based beam source intended to operate at a temperature of a few degrees Kelvin, it will be of little adverse consequence for a neon-based beam source designed to operate at temperatures approaching 20 K [22].

The temporal behavior of the CH signal is shown in Fig. 2. At long times after the ablation pulse, the optical density is observed to decrease exponentially in time, as expected for diffusion. In addition, the exponential lifetime increases linearly with helium density over the range from 4×10^{15} to 5×10^{16} cm^{-3}, indicating that the dominant loss mechanism is diffusion to the cell walls and not chemical reactions with other species produced by the ablation.

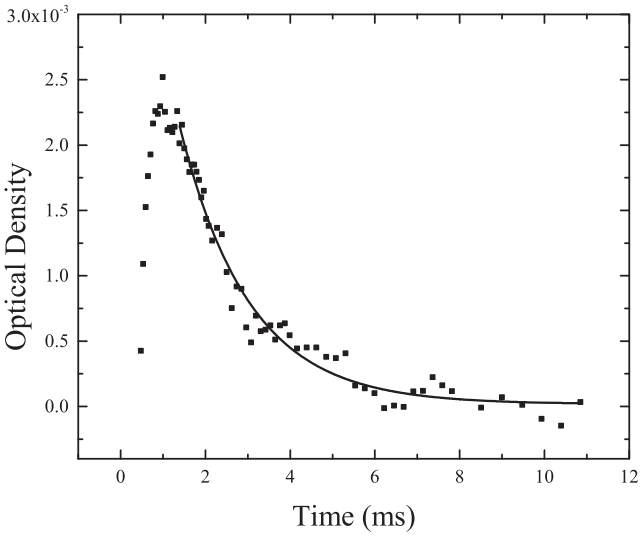

FIG. 2. Measured optical density on the Q-branch transition as a function of time after the laser ablation pulse. The experimental measurements are shown as solid squares, and the fit to an exponential is shown as a solid line; the exponential time constant is 2 ms. The data were taken at a cell temperature of 5 K, ablation energy of 0.1 J, and helium buffer gas density of 1×10^{16} cm^{-3}.

III. STARK DECELERATION OF A POSITION- AND VELOCITY-CORRELATED BEAM

Stark deceleration is a method that uses time-varying inhomogeneous electric fields to reduce the mean velocity of a molecular beam via the interaction of an electric field with a molecule's electric dipole moment (Fig. 3).

Previously, this had been realized as a spatially periodic array of high-voltage electrode pairs that create electric-field maxima along the molecular-beam path [24]. These maxima create a time-averaged potential well that periodically removes kinetic energy from the target molecules. This method has been described previously in Ref. [25]. Recently, a new method of Stark deceleration has been demonstrated in which a series of ring electrodes, with continuously varying voltages applied, creates a true moving potential well that decelerates molecules [26]. The potential well moves initially at the mean speed of the molecular beam but subsequently decreases its speed to decelerate molecules in the trapped potential well. This method has been implemented both alone [27] and in combination with a traditional decelerator [28]. The salient advantage of this "traveling-wave" decelerator is the true three-dimensional confinement of the molecules, which inhibits transverse losses during the deceleration process.

Stark deceleration of supersonic beams has been studied in great detail [25], but its application to the different beam parameters offered by a cryogenic buffer-gas source remains unexplored. Typical parameters for the two sources have been well documented [1,29,30]. For our simulations, we chose parameters listed in Table I, characteristic of a neon buffer-gas beam in the hydrodynamic expansion regime [22].

A buffer-gas source can create beams with transverse and longitudinal velocity spreads similar to those of a supersonic beam but with reduced longitudinal velocities [22]. The lower mean speed makes deceleration less technically demanding as the frequency of the changing potentials is reduced. However, the large temporal spread of buffer-gas sources creates large longitudinal position spreads, which means only a small fraction of the beam will fit inside a single potential well of the decelerator. Also, the spread in longitudinal velocity is much larger than the velocity acceptance of the decelerator.

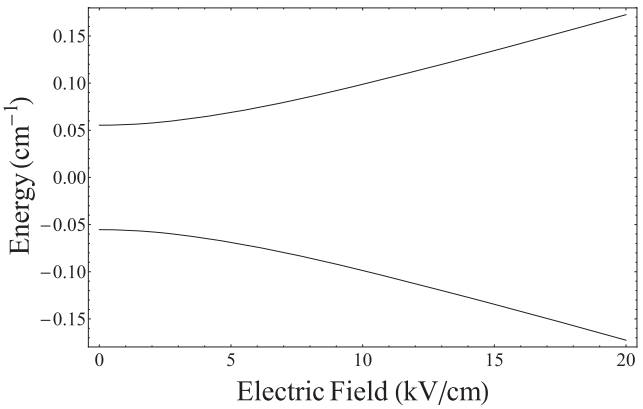

FIG. 3. Stark shift of the λ doublet states of the $^2\Pi_{\frac{1}{2}}$ energy level for $|J,M\rangle = |\frac{1}{2}, \pm\frac{1}{2}\rangle$. This calculation does not take into account coupling to higher-lying rotational levels.

TABLE I. Parameters of the buffer-gas beam used in simulations. The expansion out of the cell is assumed to be in the hydrodynamic regime. These parameters would correspond to a cell extraction time of ∼ 2 ms and a cell aperture diameter of ∼ 5 mm for a physical cell [22].

Parameter	Value
Average forward velocity	180 m/s
Longitudinal velocity spread	17 m/s (1σ)
Longitudinal position spread	10 cm (1σ)
Transverse velocity spread	21 m/s (1σ)
Transverse position spread	1.7 mm (1σ)

To address these two problems, we developed a protocol to correlate the longitudinal position and velocity of the molecular beam and to match the deceleration of the potential wells to the correlated phase-space distribution (PSD). From the parameters in Table I, it is clear that the PSD of molecules is much larger than the phase-space acceptance (PSA) of a single potential well, which is typically 8 mm wide in the position coordinate. However, after correlation, the molecules enter the decelerator over a large time interval. Over this interval, the PSA can be swept to overlap the molecular distribution as it evolves. This results in molecules being loaded into many successive wells of the decelerator and a considerable fraction of the beam being decelerated.

The correlation of the velocity and position of the molecule beam is accomplished by allowing the beam to propagate through a long electrostatic hexapole before entering the decelerator. During this propagation, the molecules with higher longitudinal speeds move ahead of the center of the packet, while the slower molecules lag behind, thus creating a position and velocity correlation [31]. The instantaneous potential well velocity is then chosen to match the velocity of arriving molecules, dynamically changing the decelerator's PSA to match the PSD of the arriving molecular beam. In this way, many wells of the decelerator can be loaded with a high density of molecules, and a significant fraction of the beam can be decelerated. This approach is illustrated schematically in Fig. 4.

To establish how the velocity of the decelerator wells should change in time, we consider the velocity of a molecule as

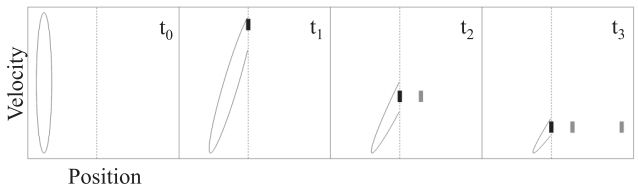

FIG. 4. Time series schematic of the molecule acceptance scheme. As the molecular packet (ellipse) approaches the decelerator entrance (represented by the dotted line), its longitudinal PSD rotates and stretches. The velocity of molecules arriving at the decelerator entrance decreases over time. If the decelerator well velocity changes in a manner that matches the changing molecule arrival velocity, molecules can be captured and decelerated in successive potential wells (rectangles).

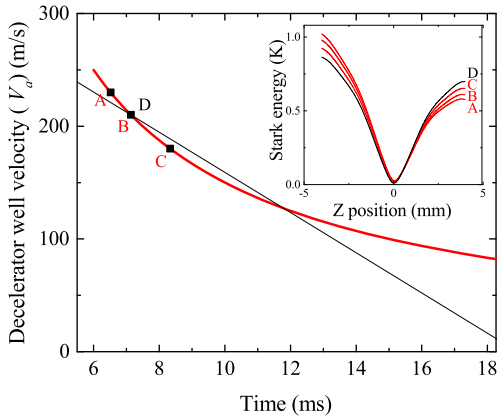

FIG. 5. (Color online) Linear and $1/t$ acceptance functions. The linear (black) curve uses a constant acceleration designed to bring an index molecule with 210 m/s velocity to a standstill with 600 decelerator rings. The nonlinear [red (gray)] curve tracks the center velocity of molecules entering the decelerator after traveling through a 1.5-m hexapole guide. The inset shows how the depth of the potential well experienced by the molecules changes with acceleration.

it enters the decelerator after being guided from the source aperture by a hexapole. In the limit of a long hexapole guide, a molecule's longitudinal speed at the decelerator entrance will vary as $v = H/t$, where H is the length of the hexapole and t is time the packet has been propagating. In this limit, one would achieve perfect coupling if the velocity of the decelerator's potential wells V_a had the same functional form. Using this exact form is impractical since changing V_a as $1/t$ requires an infinitely long decelerator to decelerate molecules to rest. What is more, because this acceptance scheme involves very large accelerations when molecules first enter the decelerator, the initial phase-space acceptance is very small [26]. A more practical deceleration protocol is a linear chirp function, which approximates the ideal acceleration function.

Because of the wide velocity spread in our beam, the optimal choice of acceleration in a linear velocity scheme is not immediately obvious. We define the acceleration through the use of an "index molecule." The index molecule velocity determines the acceleration a by

$$a = \frac{\left(V_f^2 - V_i^2\right)}{2S}, \tag{4}$$

where V_i is the velocity of the index molecule, V_f is the final velocity after deceleration, and S is the length of the decelerator. We then change the velocity of the decelerator wells according to

$$V_a(t) = -a\left(t - \frac{H}{V_i}\right) + V_i. \tag{5}$$

An example of the linear and $1/t$ acceleration functions are shown in Fig. 5. The effective longitudinal potential well is shown in the inset for various times during the deceleration. For the linear acceptance function, the acceleration is constant, and the shape of the potential well does not change during deceleration. For a $1/t$ acceptance function, the leading edge of the potential well increases as the acceleration decreases, leading to a larger PSA. We investigate the effect of these different deceleration protocols and parameters both by using three-dimensional (3D) Monte Carlo simulations and by developing a simple one-dimensional (1D) model.

IV. MOLECULAR TRAJECTORY SIMULATIONS

We begin simulations by calculating the position- and time-dependent Stark energies of a CH molecule within the decelerator using a commercial finite-element solver. Stark energies are calculated for sinusoidal voltages applied to the ring electrodes with a peak-to-peak amplitude of 24 kV. The ring electrodes have an inner diameter of 4 mm and a wire diameter of 1 mm and are spaced by 2 mm. The 4-mm-inner-diameter hexapole is modeled with an ideal potential with adjacent rods having a 400-V potential difference. The hexapole voltage was tuned in simulations for good transverse phase-space matching to the decelerator and is the same for all guide lengths. The hexapole potential also features a hard cutoff at the rod radius, outside of which molecules exit the simulation. Next, we generate a Gaussian-distributed molecule packet in all six dimensions of phase space using parameters listed in Table I, which are meant to reflect typical pulse parameters reported in the literature [1,22]. We evolve the trajectories of 40,000 molecules through the decelerator with a standard integrator and record their final position in phase space.

We can understand much of what goes on during deceleration by examination of the final molecular phase-space distribution. In Fig. 6, molecules have been decelerated from 180 to 25 m/s with a predecelerator hexapole length of 1.5 m. The final velocity of 25 m/s was chosen because it is a typical value for loading molecules into an external trap. Molecules that leave the simulation by going beyond the hexapole or decelerator ring radius have their phase-space coordinates

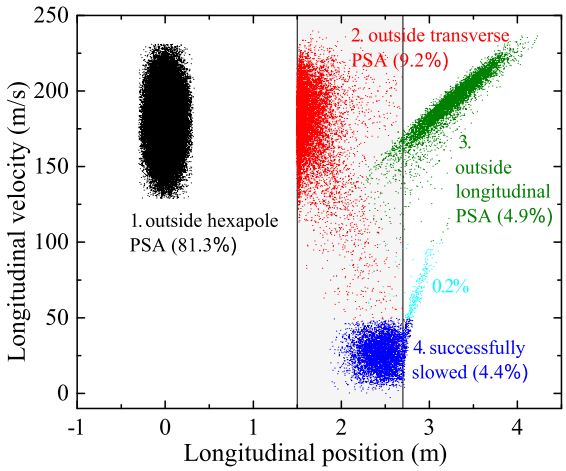

FIG. 6. (Color online) Simulated final longitudinal phase-space distribution for linear deceleration using a 1.5-m hexapole and 210 m/s index molecule. Molecules are frozen at their phase-space coordinates when they exit the simulation by moving beyond the inner diameter of the hexapole or slower or the simulation ends. The shaded region represents the location of the decelerator.

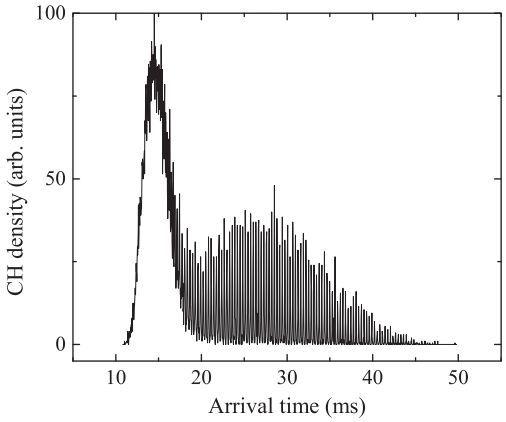

FIG. 7. Simulated time-of-flight trace for deceleration of a buffer-gas beam. The parameters are the same as those for Fig. 6. The molecules in the first broad peak have a velocity of 180 m/s. The numerous narrow peaks correspond to decelerated molecules with an average velocity of 25 m/s.

recorded, cease to evolve, and are tagged with their loss mechanism.

Because of the large aperture of the buffer-gas cell, most molecules start outside the transverse PSA of the hexapole and are thrown out immediately (group 1 points). Molecules that are not accepted into the decelerator either hit electrodes at the beginning of deceleration (group 2 points) or are longitudinally phase unstable and emerge from the decelerator undecelerated (group 3 points). There are also a small number of molecules (0.2%) that are phase stable but exit the decelerator before the wells reach the final velocity of 25 m/s. The final phase-space plot also reveals a striking consequence of working with a beam with such a large longitudinal width: the decelerated molecules are distributed over a length of ∼0.5 m. In a time-of-flight trace, the decelerated molecules arrive in dozens of packets (depending on deceleration parameters), as can be seen in Fig. 7. The time of flight shown in Fig. 7 comes from the same simulation as the one which generated the phase space in Fig. 6. The first broad peak in the time-of-flight curve corresponds to undecelerated molecules at 180 m/s; these are the same molecules as the ones shown as group 3 in Fig. 6. The group of small peaks centered at 29 ms corresponds to the decelerated molecules with an average velocity of 25 m/s and are shown as group 4 in Fig. 6. After deceleration, it may be possible to combine these molecules by loading them into a trap. This could be done by optical pumping [25,32] or by individually controlling electrostatic trap rings to lower and raise the front of the trap as molecules enter it, although this latter option would not increase phase-space density.

The full molecular dynamics calculations of molecular trajectories used to obtain the results shown in Figs. 6 and 7 have been shown to give excellent agreement with other experiments [33] and thus are good predictors of possible experiments described here. However, they are computationally demanding and thus not ideal for optimizing experimental parameters. As described below, we developed a 1D model of the beam deceleration. Although it is unable to yield absolute numbers of decelerated molecules, we have shown that it provides accurate calculations of *relative* numbers for different decelerator parameters and is much less computationally demanding than the full simulations. This is possible for a traveling-wave decelerator because of the near-perfect decoupling of longitudinal and transverse motion in the decelerating potential wells.

A. A 1D model of phase-space acceptance matching to a molecular beam

The one-dimensional model is based on the overlap between the molecular packet's PSD and the time-varying PSA of the decelerator. We neglect the transverse phase-space dimensions because the transverse acceptance does not vary significantly between the different deceleration protocols we evaluated. The PSD of the molecular packet is modeled as a bivariate Gaussian distribution $G(z,V_z,t)$, where z and V_z are the position and velocity variables. At the time the decelerator turns on t_0, the number of molecules within the PSA of the decelerator is approximated by

$$n = \int_{V_a-\Delta v/2}^{V_a+\Delta v/2} G(H,V_z,t_0)\, dV_z(t_0), \tag{6}$$

where Δv is the width of the decelerator acceptance in the velocity coordinate. Δv is a function of the acceleration used, which is the time derivative of V_a. To obtain this parameter, we first calculate the longitudinal separatrix, defined as the bounding phase-space curve which separates phase-stable from phase-unstable molecules. The maximum phase-stable velocity of a molecule depends on its position in a well, but since the model approximates acceptance as occurring only at the decelerator entrance, we average the width of the separatrix in the velocity coordinate over all positions inside the well to get just one approximate bounding velocity Δv. This parameter is shown as a function of acceleration in Fig. 8.

Because molecules continue to be loaded into the decelerator after t_0, we must integrate over all later times, resulting in the double integral for the total number of molecules decelerated given by

$$N = \int_{t_0}^{t=\infty} \int_{V_a(t)-\Delta v/2}^{V_a(t)+\Delta v/2} G(H,V_z,t)\, dV_z(t)\, dt. \tag{7}$$

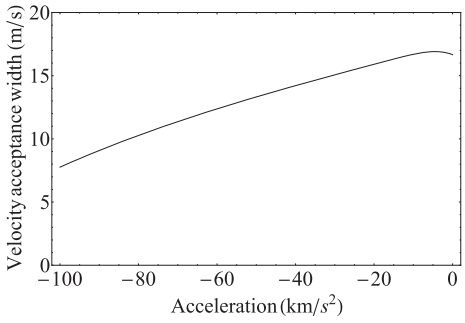

FIG. 8. The velocity acceptance width Δv used in the analytic model as a function of acceleration. For a decelerator length of 1.22 m, an acceleration of -10^5 m/s^2 is enough to decelerate an index molecule from 495 to 25 m/s.

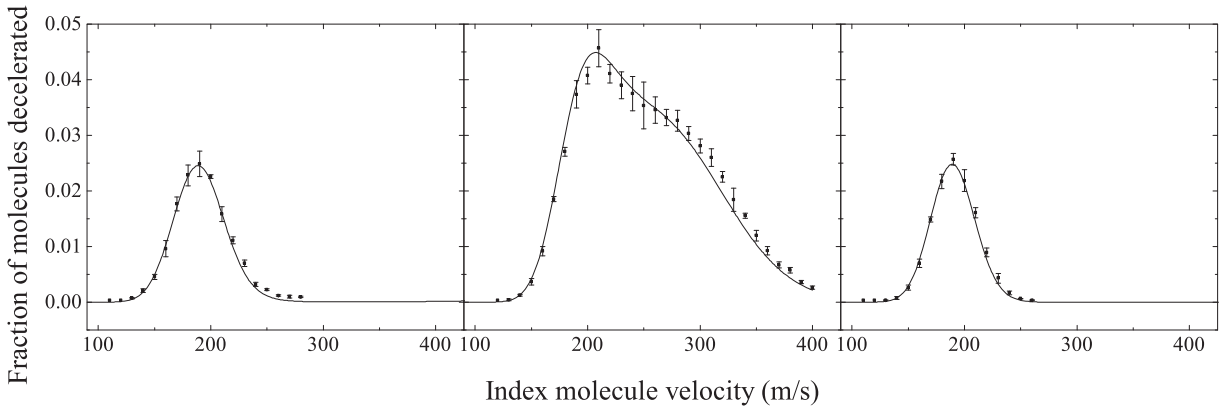

FIG. 9. The fraction of molecules decelerated using a linear chirp for hexapole guide lengths of (left) 0.5 m, (middle) 1.5 m, and (right) 4 m. The results of 3D simulations are shown as black squares, and the solid lines are 1D model predictions. All simulations used 600 decelerator rings. Each point in these plots represents separate linear chirp simulations run with a unique choice of index molecule velocity.

We note that this model neglects losses within the decelerator. This omission is justified by the 3D simulations, as seen in Fig. 6, which shows that molecules lost within the decelerator are rare. Molecules outside the transverse PSA (red points) may not be immediately lost at the decelerator entrance but can go on to have long-lived unstable orbits. Since fewer than 0.1% of molecules exhibit this behavior, a molecule that enters the decelerator is likely to reach the end. This suggests that maximizing the number of molecules in the decelerator PSA is the most promising avenue for increasing the number of molecules decelerated. The other significant approximation made by the model is that in actual deceleration experiments and in simulations, molecules are accepted in small bunches, but the 1D model incorporates this changing acceptance as a continuous function.

One-dimensional models generally fail to accurately predict the results of the deceleration process of traditional pulsed decelerators because of coupling between the longitudinal and transverse motions [34]. Three-dimensional simulations have been shown to accurately reproduce the molecular trajectories in detail [33]. We show here that for traveling-wave decelerators a much less computationally intensive 1D model reproduces the results of the full 3D simulations.

B. Results

Figure 9 shows the results of simulations and the 1D model for decelerating a buffer-gas beam from 180 to 25 m/s for different hexapole lengths using a linear chirp. In the simulations, varying the speed of the index molecule changes the magnitude of acceleration according to Eq. (4). In these results, the amplitude of the 1D model for a linear chirp for a 1.5-m guide has been scaled to match the simulation peak height. The model predictions for all other curves were then scaled by this same factor.

Both our model and our simulations show that for a 1.5-m hexapole, using a 210 m/s index molecule gives almost a factor of 2 improvement over the naive choice of 180 m/s. To explain this, we again consider the overlap of the PSA of the decelerator and the actual phase-space volume occupied by the molecular distribution. Qualitatively, this overlap is influenced by three factors: Δv, the time that the decelerator turns on, and how closely $V_a(t)$ approximates H/t. The first and third factors are similar for 180 and 210 m/s index molecules, but since the decelerator turns on when the index molecule arrives, using a 180 m/s index molecule means that 50% of the molecules have already passed the decelerator entrance. Using a 210 m/s index molecule decreases the number of molecules that escape the acceptance region before the decelerator turns on to 4%.

We show a visualization of the overlap between the PSD and the accepted molecules in Fig. 10. We see that for linear acceptance functions, using a 210 m/s molecule more effectively samples the high-density center of the incoming PSD, resulting in more molecules being accepted. Typically, decelerators are operated such that they turn on when the synchronous molecule, which is analogous to our index molecule, reaches the entrance of the decelerator. Figure 10 suggests that a better mode of operation could be to turn the

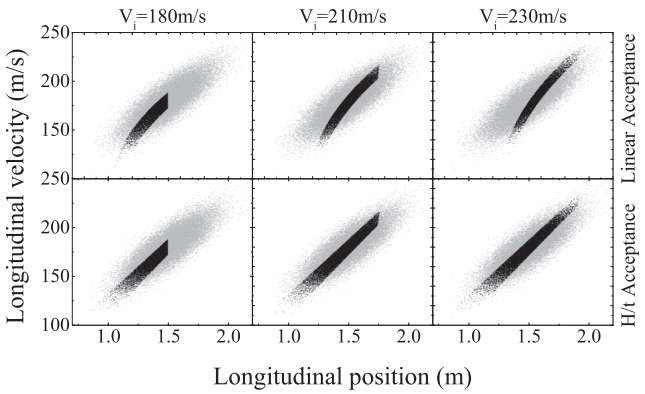

FIG. 10. A visualization of the overlap of the PSD of the molecular packet and the molecules that are accepted into the decelerator using the 1D model. The gray regions show the PSD of the molecular beam as it enters the decelerator after traveling through a 1.5-m hexapole guide. These gray regions are identical in each frame. The black regions show which molecules will be accepted after the acceptance process is complete. The top row shows the overlap for linear acceptance schemes, while the bottom row shows the overlap for H/t acceptance schemes.

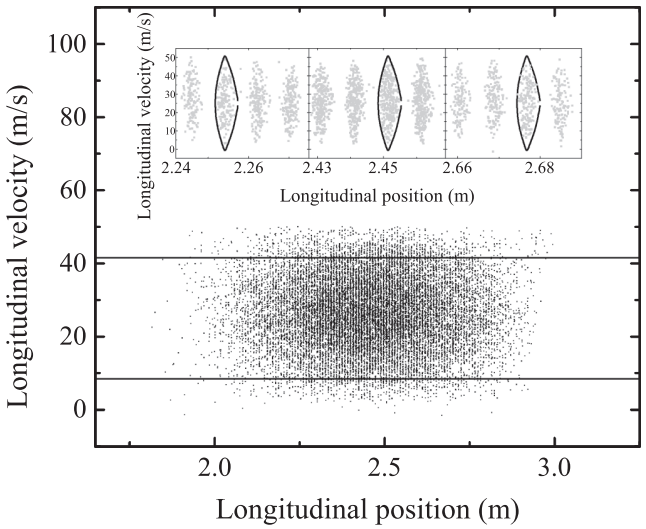

FIG. 11. A comparison of the 3D simulation results, 3D separatrices, and 1D model separatrices. One 3D separatrix is superimposed on one filled well from the beginning, middle, and end of the decelerated molecule PSD. The 1D model approximates the PSA as a continuous region in the position coordinate, so we show only the velocity boundaries (horizontal lines). The difference can only be discerned when the scale is increased to show individual wells. We see that the model separatrix does accept molecules between individual wells, which, although unphysical, results only in a consistent overestimate of how many molecules can be accepted. This accounts for the excellent agreement between the model and simulations in Fig. 9 after a constant scaling.

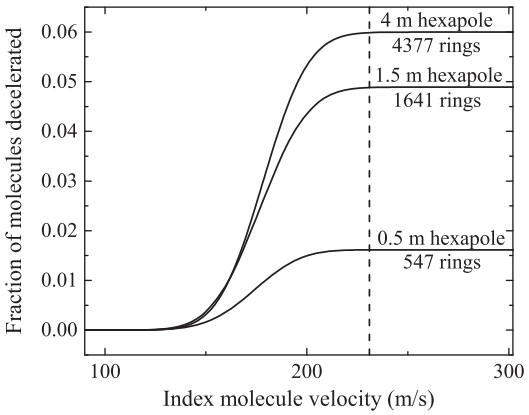

FIG. 12. One-dimensional model predictions of the fraction of molecules decelerated using the $1/t$ chirp for hexapole guide lengths of 0.5, 1.5, and 4 m. The number of rings required to decelerate the molecular pulse using a particular hexapole guide length is shown for an index molecule with a velocity of 231 m/s (dashed line), which is 180 m/s plus three times the longitudinal velocity width.

decelerator on immediately after the molecular beam exits the source. However, most molecules that are faster than the index molecule will exit the decelerator before they reach the final velocity. The number of molecules rejected this way cancels out most of the benefit of turning the decelerator on earlier. We do not show the molecules that are accepted in the 3D simulations as the difference between the 1D and 3D results are so small as to be invisible when viewed on such length scales. To illustrate the agreement between the 1D and 3D results, we compare separatrices used in the model and the simulations, as well as final phase-space positions of the simulation molecules (Fig. 11) in an individual well.

We also tested deceleration schemes using a deceleration function that matched the incoming velocity of the molecular beam (i.e., H/t), as discussed in Sec. III. The results of that model are shown in Fig. 12. For the $1/t$ chirp scheme, the index molecule sets only the time the decelerator turns on. Thus, if it turns on before most of the molecules reach the decelerator entrance, the number of molecules decelerated should be independent of the exact index molecule velocity (decelerator turn on time). This effect can be seen as a plateau in the number of molecules decelerated for large index molecule velocities (Fig. 12). Comparing the number of molecules decelerated in the plateau region for various hexapole lengths, one can see the fraction increases with hexapole length. As the molecular beam becomes more correlated in position and velocity with longer hexapole lengths, the PSA will better match the incoming molecular-beam PSD. The increase will saturate once the overlap of the PSD of the molecular beam and PSA of the decelerator is a maximum. This occurs at a fraction of 6%. (Note that 90% of the molecular beam is outside the transverse PSA regardless of the correlation length.)

The longitudinal phase-space trajectory of molecules in a H/t chirp is given by

$$V(z) = V_0 e^{1-\frac{z}{H}}, \tag{8}$$

where V_0 is the initial longitudinal velocity of a molecule. Immediately evident from these trajectories is that molecules can only be slowed to a stop with an infinitely long decelerator. The dependence on hexapole length also means that the number of rings must be considered when implementing $1/t$ chirp schemes. Essentially any length may be chosen for a linear chirp scheme, with shorter decelerators requiring larger accelerations. However, for the $1/t$ chirp, the number of rings is a fixed value, which is a function of the hexapole length and the initial and final velocities. The number of rings required for a $1/t$ chirp is given by

$$N_{\text{rings}} = \frac{H \ln \frac{V_0}{V_f}}{\Delta d}, \tag{9}$$

where Δd is the ring spacing. Thus, to realize the large gain in decelerated molecule fraction, one must build an unreasonably long Stark decelerator of several meters (Fig. 12). If the length of decelerator is fixed at 600 rings, the linear chirp produces three times more decelerated molecules than the $1/t$ chirp.

Until now, we have evaluated the deceleration schemes based on the total number of molecules decelerated. For experiments that use a slow controlled molecular beam, the total number of molecules or integrated flux is the important metric, but for experiments requiring loading molecules into a trap, density also plays a role. A list of the decelerated fraction, molecular density, and number of rings used for the different protocols is given in Table II. The densities were calculated from the simulations by counting the number of molecules in the central well of the decelerator and assuming the molecules were uniformly distributed in the well volume. We note this underestimates the true peak well density. We expect that

TABLE II. The fraction of the initial beam that is decelerated to 25 m/s, central well densities, and the number of decelerator rings used for various correlation (hexapole) lengths for both linear and $1/t$ acceptance functions. The number of rings used to decelerate using the $1/t$ chirp was set by the final velocity of 25 m/s. The density in the central well was calculated by assuming a uniform distribution within the well and thus represents a slight underestimate of the peak density.

Hexapole length	Linear deceleration			$\frac{1}{t}$ Deceleration	
(m)	Density (molecules/cm^3)	Fraction	Rings	Fraction	Rings
0.5	1.7×10^9	0.025	600	0.016	547
1.5	1.5×10^9	0.045	600	0.049	1641
4.0	8.2×10^8	0.025	600	0.060	4377

slowing protocols that make use of longer hexapoles would result in decreased well densities because the longitudinal phase-space distribution spreads during the flight time in the hexapole. This idea is borne out in the case of linear slowing protocols; the peak density decreased for the longest hexapole length, although the decrease is not very significant over the range explored.

V. CONCLUSIONS

We have created an intense source (2×10^{11}/ablation pulse) of ground-state CH radicals via buffer-gas cooling of a laser-ablated plume of iodoform. Using previously published cell extraction measurements, we estimated the parameters of a molecular beam that could be created from this buffer-gas source. We have shown that this extended pulse can be efficiently decelerated in a traveling-wave Stark decelerator by first correlating the position and velocity of molecules in the beam by guiding in an electrostatic hexapole. By optimizing this protocol using both 3D trajectory simulations and a 1D model we are able to decelerate 5% of the molecules in the initial beam. The 1D model allows rapid exploration of a large parameter space of deceleration protocols and allows for understanding of the dynamics of matching the phase-space distribution of the beam with the phase-space acceptance of the decelerator. In the near future, we hope to be able to physically combine the buffer-gas source with the traveling-wave decelerator to explore combining the individual wells into a single electrostatic trap achieving high density and molecule number, which will allow for precise studies of collisions and reactions of CH radicals.

ACKNOWLEDGMENTS

This material is based upon work supported by the National Science Foundation under Grants No. PHY 0900190, No. 1125844, No. 0748742, and No. 1265905 and by the Air Force Office of Scientific Research under Grants No. FA9550-09-1-0588 and No. FA9550-12-1-0182. We gratefully acknowledge helpful discussions with John M. Doyle.

[1] N. R. Hutzler, H.-I. Lu, and J. M. Doyle, Chem. Rev. **112**, 4803 (2012).
[2] Z. Li and E. J. Heller, J. Chem. Phys. **136**, 054306 (2012).
[3] A. C. Vutha, W. C. Campbell, Y. V. Gurevich, N. R. Hutzler, M. Parsons, D. Patterson, E. Petrik, B. Spaun, J. M. Doyle, G. Gabrielse, and D. DeMille, J. Phys. B **43**, 074007 (2010).
[4] M. R. Tarbutt, B. E. Sauer, J. J. Hudson, and E. A. Hinds, New J. Phys. **15**, 053034 (2013).
[5] S. Truppe, R. Hendricks, S. Tokunaga, H. Lewandowski, M. Kozlov, C. Henkel, E. Hinds, and M. Tarbutt, Nat. Commun. **4**, 2600 (2013).
[6] D. Gerlich and M. Smith, Phys. Scr. **73**, C25 (2006).
[7] L. D. Carr, D. DeMille, R. V. Krems, and J. Ye, New J. Phys. **11**, 055049 (2009).
[8] J. F. Barry, E. S. Shuman, E. B. Norrgard, and D. DeMille, Phys. Rev. Lett. **108**, 103002 (2012).
[9] Hsin-I Lu, I. Kozyryev, B. Hemmerling, J. Piskorski, and J. M. Doyle, Phys. Rev. Lett. **112**, 113006 (2014).
[10] M. T. Bell and T. P. Softley, Mol. Phys. **107**, 99 (2009).
[11] R. A. Brownsword, I. R. Sims, I. W. M. Smith, D. W. A. Stewart, A. Canosa, and B. R. Rowe, Astrophys. J. **485**, 195 (1997).
[12] P. Maksyutenko, F. Zhang, X. Gu, and R. I. Kaiser, Phys. Chem. Chem. Phys. **13**, 240 (2011).
[13] I. W. Smith, Annu. Rev. Astron. Astrophys. **49**, 29 (2011).
[14] F. Zhang, P. Maksyutenko, and R. I. Kaiser, Phys. Chem. Chem. Phys. **14**, 529 (2012).
[15] J.-C. Loison and A. Bergeat, Phys. Chem. Chem. Phys. **11**, 655 (2009).
[16] N. Fitch, D. Esteves, M. Fabrikant, T. Briles, Y. Shyur, L. Parazzoli, and H. Lewandowski, J. Mol. Spectrosc. **278**, 1 (2012).
[17] M.-J. Lu, K. S. Hardman, J. D. Weinstein, and B. Zygelman, Phys. Rev. A **77**, 060701(R) (2008).
[18] J. Butler, L. Goss, M. Lin, and J. Hudgens, Chem. Phys. Lett. **63**, 104 (1979).
[19] R. Kepa, A. Para, M. Rytel, and M. Zachwieja, J. Mol. Spectrosc. **178**, 189 (1996).
[20] M. C. McCarthy, S. Mohamed, J. M. Brown, and P. Thaddeus, Proc. Natl. Acad. Sci. USA **103**, 12263 (2006).
[21] J. Luque and D. R. Crosley, J. Chem. Phys. **104**, 3907 (1996).
[22] N. R. Hutzler, M. F. Parsons, Y. V. Gurevich, P. W. Hess, E. Petrik, B. Spaun, A. C. Vutha, D. DeMille, G. Gabrielse, and J. M. Doyle, Phys. Chem. Chem. Phys. **13**, 18976 (2011).
[23] S. M. Skoff, R. J. Hendricks, C. D. J. Sinclair, J. J. Hudson, D. M. Segal, B. E. Sauer, E. A. Hinds, and M. R. Tarbutt, Phys. Rev. A **83**, 023418 (2011).

[24] H. L. Bethlem, G. Berden, and G. Meijer, Phys. Rev. Lett. **83**, 1558 (1999).

[25] S. Y. T. van de Meerakker, H. L. Bethlem, N. Vanhaecke, and G. Meijer, Chem. Rev. **112**, 4828 (2012).

[26] A. Osterwalder, S. A. Meek, G. Hammer, H. Haak, and G. Meijer, Phys. Rev. A **81**, 051401 (2010).

[27] N. E. Bulleid, R. J. Hendricks, E. A. Hinds, S. A. Meek, G. Meijer, A. Osterwalder, and M. R. Tarbutt, Phys. Rev. A **86**, 021404 (2012).

[28] M. Quintero-Pérez, P. Jansen, T. E. Wall, J. E. van den Berg, S. Hoekstra, and H. L. Bethlem, Phys. Rev. Lett. **110**, 133003 (2013).

[29] S. E. Maxwell, N. Brahms, R. deCarvalho, D. R. Glenn, J. S. Helton, S. V. Nguyen, D. Patterson, J. Petricka, D. DeMille, and J. M. Doyle, Phys. Rev. Lett. **95**, 173201 (2005).

[30] N. E. Bulleid, S. M. Skoff, R. J. Hendricks, B. E. Sauer, E. A. Hinds, and M. R. Tarbutt, Phys. Chem. Chem. Phys. **15**, 12299 (2013).

[31] S. A. Meek, H. Conrad, and G. Meijer, Science **324**, 1699 (2009).

[32] Hsin-I Lu, I. Kozyryev, B. Hemmerling, J. Piskorski, and J. M. Doyle, Phys. Rev. Lett. **112**, 113006 (2014).

[33] L. P. Parazzoli, N. Fitch, D. S. Lobser, and H. J. Lewandowski, New J. Phys. **11**, 055031 (2009).

[34] S. Y. T. van de Meerakker, N. Vanhaecke, H. L. Bethlem, and G. Meijer, Phys. Rev. A **73**, 023401 (2006).